Journal of the Energy Institute xxx (xxxx) xxx

Contents lists available at ScienceDirect

Journal of the Energy Institute

journal homepage: www.journals.elsevier.com/journal-of-the-energy-institute

La-doped cobalt supported on mesoporous alumina catalysts for improved methane dry reforming and coke mitigation

Ngoc Thang Tran [a, b], Quyet Van Le [c], Nguyen Van Cuong [b], Trinh Duy Nguyen [d], Nguyen Huu Huy Phuc [e], Pham T.T. Phuong [f], Minhaj Uddin Monir [g], Azrina Abd Aziz [h], Quang Duc Truong [i], Sumaiya Zainal Abidin [a, **], Sonil Nanda [j], Dai-Viet N. Vo [d, *]

[a] Faculty of Chemical and Process Engineering Technology, College of Engineering Technology, Universiti Malaysia Pahang, Lebuhraya Tun Razak, 26300, Gambang, Kuantan, Pahang, Malaysia
[b] Faculty of Chemical Engineering, Industrial University of Ho Chi Minh City, 12 Nguyen Van Bao St, Go Vap, Ho Chi Minh City, 7000, Viet Nam
[c] Institute of Research and Development, Duy Tan University, Da Nang, 550000, Viet Nam
[d] Center of Excellence for Green Energy and Environmental Nanomaterials (CE@GrEEN), Nguyen Tat Thanh University, 300A Nguyen Tat Thanh, District 4, Ho Chi Minh City, 755414, Viet Nam
[e] Department of Electrical and Electronic Information Engineering, Toyohashi University of Technology, 1-1 Hibarigaoka, Tempaku, Toyohashi, Aichi, 441-8580, Japan
[f] Institute of Chemical Technology, Vietnam Academy of Science and Technology, 1 Mac Dinh Chi Str., Dist.1, Ho Chi Minh City, Viet Nam
[g] Department of Petroleum and Mining Engineering, Jashore University of Science and Technology, Jashore, 7408, Bangladesh
[h] Faculty of Civil Engineering Technology, Universiti Malaysia Pahang, 26300, Gambang, Malaysia
[i] Institute of Multidisciplinary Research for Advanced Materials, Tohoku University, Sendai, 980-8577, Japan
[j] Department of Chemical and Biological Engineering, University of Saskatchewan, Saskatoon, Saskatchewan, Canada

ARTICLE INFO

Article history:
Received 1 November 2019
Received in revised form
16 January 2020
Accepted 20 January 2020
Available online xxx

Keywords:
Methane dry reforming
Cobalt catalyst
La_2O_3
Syngas
Mesoporous alumina
Hydrogen

ABSTRACT

The promotional La_2O_3 effect on the physicochemical features of mesoporous alumina (MA) supported cobalt catalyst and its catalytic performance for methane dry reforming (MDR) was examined at varied temperature and stoichiometry feedstock. The Co_3O_4 nanoparticles were evidently scattered on fibrous mesoporous alumina with small crystal size of 8–10 nm. The promotion behavior of La_2O_3 facilitated H_2-reduction by providing higher electron density and enhanced oxygen vacancy in 10%Co/MA. The addition of La_2O_3 could reduce the apparent activation energy of CH_4 consumption; hence, increasing CH_4 conversion up to 93.7% at 1073 K. The enhancement of catalytic activity with La_2O_3 addition was also due to smaller crystallite size, alleviated H_2-reduction and the basic character of La_2O_3. Lanthanum dioxycarbonate transitional phase formed *in situ* during MDR was accountable for mitigating deposited carbon via redox cycle for 17–30% relying on reaction temperature. Additionally, the oxygen vacancy degree increased to 73.3% with La_2O_3 promotion. The variation of H_2/CO ratios within 0.63–0.99 was preferred for downstream generation of long-chain olefinic hydrocarbons.

1. Introduction

The increasingly excessive consumption of fossil-based energies because of growing industrial production, transportation and global population has led to many serious issues relating to the energy security, petroleum depletion, global warming, air pollution and unhealthy human living environment [1–3]. Thus, CO_2 mitigation and the exploration of petroleum-substituted fuels are currently required worldwide. Methane dry reforming (MDR, Eq. (1)) appears to be a promising approach since it converts two greenhouse gases (CO_2 and CH_4, main causes of global warming) to the valuable mixture of CO and H_2, so-called syngas [4,5]. Additionally, syngas-derived H_2 could be used as a standalone, green and efficient fuel in fuel cells and hydrogen car as well as feedstock in petrochemical industry since it has a high energy density about 120.7 kJ g^{-1} [6] and its combustion only induces H_2O by-product [7,8].

* Corresponding author.
** Corresponding author.
E-mail addresses: sumaiya@ump.edu.my (S.Z. Abidin), vndviet@ntt.edu.vn, daivietvnn@yahoo.com, vo.nguyen.dai.viet@gmail.com (D.-V.N. Vo).

https://doi.org/10.1016/j.joei.2020.01.019
1743-9671/

$$CO_2 + CH_4 \rightarrow 2H_2 + 2CO \qquad (\Delta H_{298\ K} = +274\ kJ\ mol^{-1}) \quad (1)$$

Noble metals such as Pd, Pt and Rh and Ni transition metal are broadly used for MDR [9,10]. Even though precious metals perform high MDR activity and stability, these metals are rare and expensive and thus are unsuitable for industrial scale [11]. Additionally, Ni-based catalysts could easily involve in undesirable catalytic deactivation due to coke formation and metal sintering induced by high MDR reaction temperature [12]. Thus, designing a cost-effective catalyst with high activity and coke mitigation is the main concern in MDR industry.

In recent years, Co-based materials have emerged as potential and alternative catalysts for the industrial reforming processes owing to their high thermal stability, abundant resources and great activity [13,14]. Additionally, Co catalysts are reportedly less prone to metal sintering and carbon deposition in comparison with Ni-based catalysts [15]. Apart from active metals, the variety of supports and promoters plays efficient and important roles in the prevention of catalyst deterioration.

In fact, mesoporous supports, especially alumina, have been widely employed to enhance metal dispersion and provide the confinement effect for active metals to prevent them from agglomeration due to their ordered mesoporous structure [16,17]. Unlike other mesoporous siliceous supports such as MCM-41 and SBA-15 having mesopore collapse induced by high MDR reaction temperature [18], Ma et al. studied Al_2O_3-supported bimetallic Pd–Ni catalysts for MDR and reported that Al_2O_3 support has great thermal stability resisting toward thermal sintering and high surface area beneficial for nanoparticle dispersion [16]. The basic character of rare-earth metal oxides has reportedly improved the adsorption of CO_2 reactant, thereby increasing carbon gasification from catalyst surface [19]. Lanthanum oxide with basic properties and high oxygen storage capacity was recently found to enhance carbon resistance in various reforming processes [4,19,20]. The dispersion of Co active metal on mesoporous Al_2O_3 with La_2O_3 promotion could exhibit high reforming activity and coke resilience, but this potential metal oxide combination has not been previously examined for MDR to the best of our knowledge. Since the above-mentioned catalytic recipe could possess outstanding performance and carbon resistance and was not explored before in literature, it is crucial to examine its catalytic behavior in MDR at varied reaction temperature. Thus, the objective of this work is to scrutinize the promotional La_2O_3 effects on Co/MA catalyst for enhanced MDR in terms of H_2 generation and coke mitigation. The influence of reaction temperature ranging from 973 K to 1073 K on reactant conversions and product yields was also examined in this study.

2. Materials and methods

2.1. Catalyst synthesis

Alumina support was synthesized by dissolving 0.98 g of tri-block-poly (ethylene glycol)-block-poly (propylene glycol)-block-poly (ethylene glycol), Pluronic® P-123 ($EO_{20}PO_{70}EO_{20}$ with mean molecular weight of 5800 purchased from Sigma-Aldrich, St. Louis, Missouri, US) in a binary solvent mixture (14.7 ml) containing 25% water and 75% ethanol by volume using a magnetic stirrer. The solution was vigorously mixed for 30 min at 303 K, followed by sequentially adding 3.68 g of aluminum nitrate nonahydrate, $Al(NO_3)_3.9H_2O$ (98%, Merck Millipore) and 1.6 ml of hydrochloric acid fuming (37%, Merck Millipore) with continuously stirring for the next 1 h. Hydrothermal treatment was performed in a Teflon-lined stainless autoclave for 24 h at 373 K. The resultant mixture was slowly evaporated at 333 K in Memmert UF1060 oven (Schwabach, Germany) for 48 h. Later, the obtained jelly liquid was exposed to a muffle furnace (Carbolite, CWF 1200, Sheffield, UK) for 5 h calcination at 1073 K and 1 K min^{-1} to yield mesoporous alumina denoted as MA.

In our previous ethanol dry reforming studies, the optimal composition for promoter and active metal was 3% and 10% in this order [21,22]. Thus, these empirical loadings were applied again in this study for selecting the recipe of promoted catalyst. Particularly, 3%La–10%Co/MA was prepared using an incipient wetness co-impregnation method in which a solution of 0.57 g of $Co(NO_3)_2.6H_2O$ (Sigma-Aldrich, St. Louis, Missouri, US) metal precursor and 0.11 g of $La(NO_3)_3.6H_2O$ promoter source (Merck KGaA, Darmstadt, Germany) in 0.5 ml of anhydrate ethanol was mixed with 1 g of as-prepared MA support for 1 h. The impregnated solid was instantly dried at 373 K overnight in oven and calcined at 873 K for 5 h with heating rate of 1 K min^{-1} in furnace. The incipient wetness impregnation approach was also implemented for un-promoted 10%Co/MA synthesis using the analogous above-mentioned procedure without promoter solution addition.

2.2. Catalyst characterization

X-ray diffraction analysis was performed on Miniflex 600 spectrometer (Rigaku, Tokyo, Japan) with Cu radiation source ($\lambda = 1.5418$ Å). All the diffraction patterns were recorded at scanning range of 3-80° with step size of 0.02° and scan speed of 1° min^{-1}. The Joint Committee on Power Diffraction Standards (JCPDS) database was used as references for peak identification [23] and the crystallize size was calculated using Scherrer's equation (see Eq. (2)) based on the most intense peak [24].

$$d_{Co_3O_4} = \frac{0.94 \times \lambda}{\beta \times \mathrm{Cos}\,\theta} \quad (2)$$

where θ is Bragg angle and β is line broadening at half the maximum intensity.

The automated gas adsorption device (Tristar II 3020, Micrometrics, USA), employing liquefied nitrogen at 77 K, was used to examine sample textural properties. Prior to any tests, the specimen was de-gassed in N_2 flow at 573 K for 1 h to remove traced impurities and moisture. H_2-thermal programmed reduction (H_2-TPR) was conducted on the AutoChem II-2920 apparatus (Micromeritics, Georgia, USA). For each run, about 50 mg of catalyst placed at the center of a quartz U-tube was purged in N_2 at 373 K and 30 min followed by reduction step in 10%H_2/N_2 (50 ml min^{-1}) with programmed temperature from 373 K to 1173 K using 10 K min^{-1}. Reduced sample was kept constant at 1173 K for 30 min before cooling down to ambient temperature in N_2.

Thermal programmed oxidation (TPO) was performed in a TGA Q500 series apparatus from (TA Instruments, Newcastle, DE, USA). The specimen was first dehydrated at 373 K under N_2 flux (100 ml min^{-1}) for 30 min. The pretreated sample was then exposed to the premixed flow of 20 ml min^{-1} O_2 and 80 ml min^{-1} N_2 whilst temperature was raised from 373 to 1023 K with a rate of 10 K min^{-1}, followed by isothermal oxidation at 1023 K for 30 min. Raman spectroscopy was carried out using a NRS-3100 spectrophotometer (JASCO, Tokyo, Japan) at room temperature. The excitation source was the 532 nm solid-state primary laser. X-ray photoelectron spectroscopy (XPS) was conducted for the used samples on ULVAC-PHI 5000 Series equipment (VersaProbe II, Chigasaki, Japan) fitted with Al Kα X-ray radiation at hν = 1486.6 eV. The electron microscopy at high resolution (HRTEM) was performed using a TOPCOM EM-002B microscope (Japan) at 200 kV.

Please cite this article as: N.T. Tran et al., La-doped cobalt supported on mesoporous alumina catalysts for improved methane dry reforming and coke mitigation, Journal of the Energy Institute, https://doi.org/10.1016/j.joei.2020.01.019

2.3. Methane dry reforming procedure

The as-prepared catalysts were assessed for MDR from 973 to 1073 K with stoichiometry ratio at 0.1 MPa. For each run, about 0.1 g of catalyst was loaded into the center of fixed-bed reactor with length and outer diameter of 17 in. and 3/8 in., respectively and mounted by quartz wool. The delivery rates of reactants and nitrogen diluent gas were individually controlled by mass flow controllers (Alicat Scientific, Tucson, AZ, USA). All the gases were well mixed before entering the reactor and the total space velocity was fixed at 36 L g_{cat}^{-1} h^{-1} for all runs.

Prior to catalytic evaluation, H_2 activation was performed *in situ* at 1073 K for 1 h using 50%H_2/N_2 (60 ml min^{-1}) mixture. All gaseous products discharged from reactor bottom were recorded by an online thermal conductivity detector (TCD) in Agilent 6890 Gas Chromatography (Agilent Technologies, Santa Clara, CA, USA). Key reaction metrics, namely, conversion (X_j with j: CH_4 or CO_2), yield (Y_{CO} and Y_{H2}) and H_2/CO proportion were estimated using the corresponding Eqs. (3)–(6) according to the inlet, Q^{in} and outlet, Q^{out} flow rates (mol s^{-1}).

$$X_j(\%) = \frac{Q_j^{in} - Q_j^{out}}{Q_j^{in}} \times 100\% \quad (3)$$

$$Y_{CO}(\%) = \frac{Q_{CO}^{out}}{Q_{CH_4}^{in} + Q_{CO_2}^{in}} \times 100\% \quad (4)$$

$$Y_{H_2}(\%) = \frac{Q_{H_2}^{out}}{2Q_{CH_4}^{in}} \times 100\% \quad (5)$$

and

$$\frac{H_2}{CO} = \frac{Q_{H_2}^{out}}{Q_{CO}^{out}} \quad (6)$$

3. Results and discussion

3.1. Characterization of catalyst

3.1.1. X-ray diffraction analysis

The XRD patterns of MA support, 10%Co/MA and 3%La−10%Co/MA are illustrated in Fig. 1. The diffraction peaks at 2θ of 37.40°, 39.58°, 45.96°, 60.76°, 67.02° and 77.10° appeared in all sample patterns were ascribed to γ-Al_2O_3 support (JCPDS card No. 04−0858) [25], whereas the peaks at 31.32°, 37.03°, 44.88°, and 55.82° 2θ corresponded to the existence of cobalt oxide in form of Co_3O_4 for both catalysts (JCPDS card No. 74−2120) [26]. The unavoidable formation of cobalt aluminate spinel, $CoAl_2O_4$ in both specimens was also confirmed by the appearance of peaks at 59.62°, and 65.42° (JCPDS card No. 82−2246) [20,27], indicative of great interaction amid support and metal. Notably, the typical diffraction peaks of La_2O_3 phase at 2θ of 29.87° and 53.42° (JCPDS card No. 83−1355) [28] were not detected in the XRD profile of 3% La−10%Co/MA (Fig. 1(c)) suggesting that the highly dispersed La_2O_3 promoter on catalyst surface could possess nano-size less than the XRD detection limit in agreement with other studies [29].

As shown in Table 1, the Co_3O_4 crystallite size of La-promoted sample possesses a smaller dimension (7.7 nm) compared to the unpromoted counterpart (9.2 nm). The decrease in the crystallite size was considered as a result of dilution phenomena in which La particles could assist Co_3O_4 interspersion during the impregnation step, thus consequently preventing metal agglomeration [20]. The smaller Co_3O_4 nanoparticles could induce a greater active metal surface area and improve coke suppression [30].

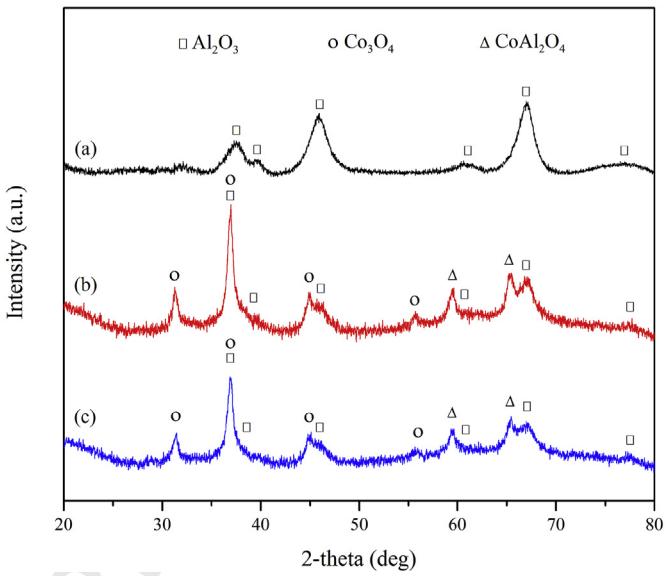

Fig. 1. XRD profiles of (a) MA, (b) 10%Co/MA, and (c) 3%La−10%Co/MA.

3.1.2. Textural properties

The N_2 adsorption-desorption behaviors of MA, 10%Co/MA and 3%La−10%Co/MA are shown in Fig. S1 (Supplementary data). All isotherm curves of measured materials were categorized as Type-IV in conjunction with the characteristic H1 hysteresis loop according to the IUPAC classifications. These typical features were attributed to mesoporous materials with cylindrical pore frameworks [31]. Although the quantity of N_2 adsorbed was dropped with Co and La additions, the constant shape of three isotherm plots and the identical H1 hysteresis loops starting at relative pressure, P/P^0 of 0.5 could be indicative of the well-preserved structure of mesoporous Al_2O_3 support after metals loading. The unchanged structure of catalysts in comparison with MA support was reasonably because of rigorously thermal support pretreatment at 1073 K prior to impregnation. Thus, the stable MA support could resist to structural alteration and retain its mesoporous feature during catalyst preparation.

The pore size distributions of support and catalysts were estimated from the experimental desorption curves by Barrett-Joyner-Halenda (BJH) approach as depicted in Fig. S2 (see Supplementary data). The distribution of pore diameters for all samples owned analogous shapes with peaks at around 6 nm and varied within 2−12 nm. The similar pore size distribution for support and catalysts further validates the unaltered support structure during metal impregnation.

The detailed textural characters of all samples are summarized in Table 1. The total pore volume and BET surface area of MA were about 0.28 cm^3 g^{-1} and 173.4 m^2 g^{-1}, respectively. The BET surface area of synthesized MA in this study is comparable with results reported for commercial Al_2O_3 supports supplied by Sasol (Puralox SCCa-150/200) [32] or Sigma-Aldrich Chemicals [19] and self-prepared Al_2O_3 supports in other works [33] signifying the successful preparation of MA. These physical attributes were reduced with Co addition, indicating the successful metal diffusion on MA surface. In comparison between promoted and unpromoted catalysts, the textural values including BET surface area and total pore volume only had a slight deviation. This could affirm the high

Please cite this article as: N.T. Tran et al., La-doped cobalt supported on mesoporous alumina catalysts for improved methane dry reforming and coke mitigation, Journal of the Energy Institute, https://doi.org/10.1016/j.joei.2020.01.019

Table 1
Physical properties of MA, 10%Co/MA, and 3%La−10%Co/MA.

Material	Specific BET surface area ($m^2\ g^{-1}$)	Total pore volume ($cm^3\ g^{-1}$)	Average pore diameter (nm)	Average Co_3O_4 crystallite size[a] (nm)
MA	173.4	0.28	6.48	-
10%Co/MA	141.9	0.22	6.28	9.2
3%La−0%Co/MA	136.4	0.21	6.30	7.7

[a] Crystallite size of Co_3O_4 calculated from Scherrer equation at 2θ angle of 37.03° after peaks of Al_2O_3 phase were subtracted from XRD patterns of both catalysts.

dispersion of both La_2O_3 and Co_3O_4 particles during co-impregnation. The BET surface area of 10%Co/MA (141.9 $m^2\ g^{-1}$) and 3%La−10%Co/MA (136.4 $m^2\ g^{-1}$) is also analogous to findings from Fayaz et al. [32].

3.1.3. H_2-thermal programmed reduction

The H_2-reduction behaviors of samples were examined by H_2-TPR as displayed in Fig. 2. Regardless of the catalysts, both Co_3O_4 and $CoAl_2O_4$ forms were reduced to Co^0 metallic phase as evidenced by three distinct peaks (P1, P2 and P3). Particularly, these peaks belong to the reduction of Co (III) oxide to Co (II) oxide (peak P1, Eq. (7)), Co (II) oxide to Co (0) metal (peak P2, Eq. (8)) and Co (II) in $CoAl_2O_4$ spinel to Co (0) phase (peak P3, Eq. (9)) [34].

$$Co_3O_4 + H_2 \rightarrow 3CoO + H_2O \quad (7)$$

$$CoO + H_2 \rightarrow Co^0 + H_2O \quad (8)$$

$$CoAl_2O_4 + H_2 \rightarrow Co^0 + Al_2O_3 + H_2O \quad (9)$$

Notably, all reduction peaks of 3%La−10%Co/MA were shifted to lower temperature zones, especially for the first peak P1 with about 72 °C temperature decline in comparison with 10%Co/MA counterpart as summarized in Table 2. This behavior could signify that cobalt particles reduction was facilitated with the presence of La_2O_3 promoter as it enhanced electron intensity on catalyst surface [35,36]. The eased reduction process with La_2O_3 promoter could be indicative of greater quantity of Co^0 active sites on 3%La−10%Co/MA and hence better catalytic performance.

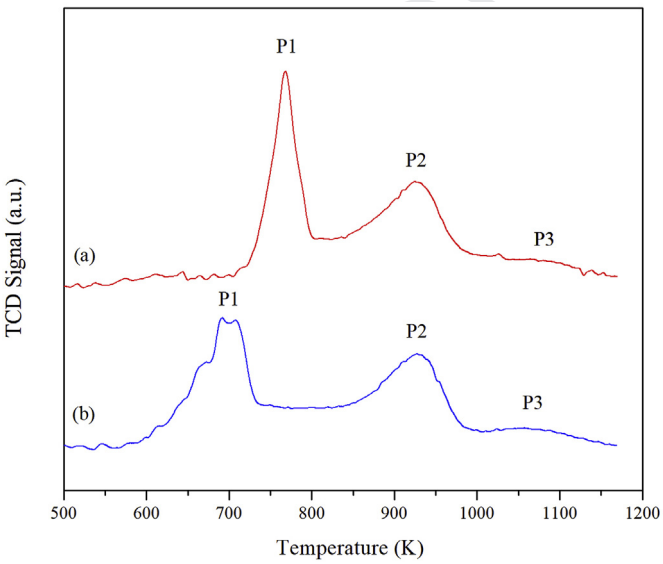

Fig. 2. H_2-TPR profiles of (a) 10%Co/MA, and (b) 3%La−10%Co/MA.

Table 2
Summary of peak reduction temperatures during H_2-TPR.

Catalyst	Peak temperature (K)		
	P1	P2	P3
10%Co/MA	768	913	1084
3%La−10%Co/MA	696	909	1077

3.2. Methane dry reforming evaluation

The MDR performance over 10%Co/MA and 3%La−10%Co/MA at different temperatures including 973 K, 1023 K and 1073 K is shown in Figs. 3 and 4. For both catalysts, the conversion of CH_4 and CO_2 (Fig. 3) and product yields (Fig. 4) increased substantially along with rising temperature because of the endothermic attribute of MDR greatly favored at high temperature [4,37]. In general, CO_2 and CH_4 conversions were increased from the corresponding 82.4% and 78.8%−93.2% and 93.7% as temperature was elevated from 973 to 1073 K on 3%La−10%Co/MA (see Fig. 3). Additionally, for 3%La−10%Co/MA, both H_2 and CO yields were heightened with temperature and reached to 84.2% and 84.1%, respectively as displayed in Fig. 4.

Irrespective of the operating temperatures, MDR catalytic performance (*viz.*, conversion and yield) on 3%La−10%Co/MA was always higher than that of 10%Co/MA (see Figs. 3 and 4), emphasizing the essential role of La_2O_3 dopant in boosting MDR performance. The enhanced performance resulted from the synergic effects of La_2O_3 promoter such as smaller crystalline size (see Table 1) and eased H_2-reduction (Fig. 2), thereby increasing the number of active sites. The basic nature of La_2O_3 also offered a significant contribution to improved CO_2 reactant adsorption and C=O bond cleavage [38,39].

The apparent activation energy (E_a) for CH_4 consumption in MDR is normally employed to validate the catalytic reactiveness and it is broadly determined using Arrhenius plot of $\ln(-r_{CH_4})$ *vs.* $1/T$ to avoid the complete acquisition of reaction kinetics [40,41]. As seen in Fig. 5, the E_a values for these catalysts were estimated within the temperature range of 973−1073 K at stoichiometric feed ratio with high correlation coefficients, $R^2 > 0.99$. Particularly, the E_a value for 3%La−10%Co/MA was roughly 19.11 kJ mol^{-1}, a half of value for 10%Co/MA counterpart (43.48 kJ mol^{-1}). The smaller E_a value of 3%La−10%Co/MA could imply the easier initiation of MDR requiring less energy for rupturing C−H and C=O bonds on this catalyst. Thus, the E_a trend further clarified the superior 3%La−10%Co/MA activity over 10%Co/MA.

As seen in Fig. 6, regardless of catalyst types and reaction temperatures, H_2/CO ratio was always less than the theoretically stoichiometric proportion of 1 (see Eq. (1)) provoked by the concurrent existence of the reverse water-gas shift (RWGS, Eq. (10)) reaction in MDR [4]. Thus, the low ratio of H_2 to CO from 0.63 to 0.99 is ideal for the generation of long-chain olefinic hydrocarbons in Fischer-Tropsch process [4,42].

$$CO_2 + H_2 \rightleftarrows CO + H_2O \quad (\Delta H_{298\ K} = +41\ kJ\ mol^{-1}) \quad (10)$$

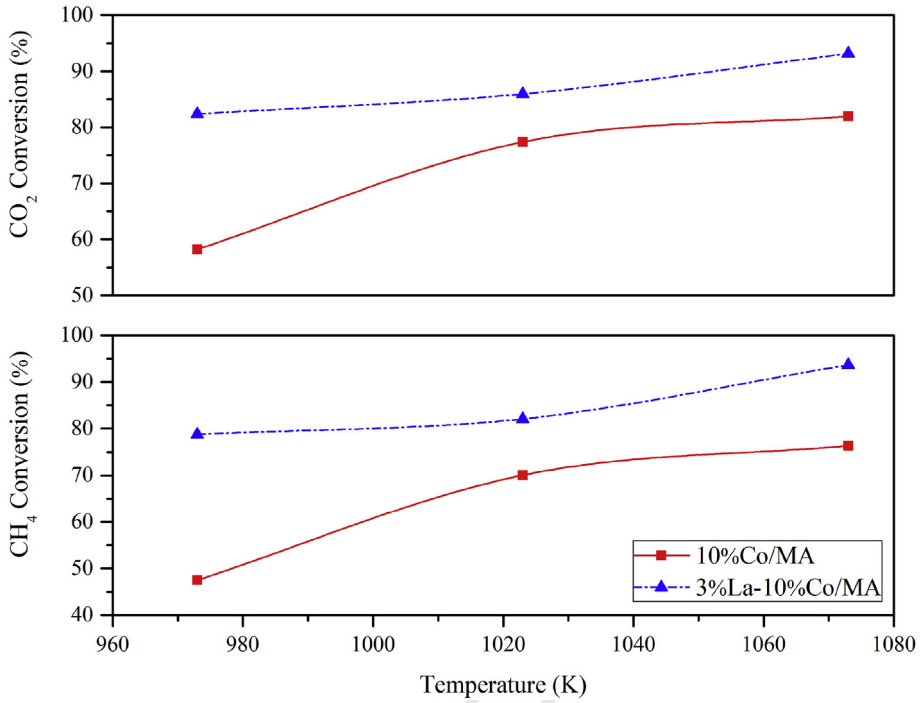

Fig. 3. Effect of temperature on CO_2 and CH_4 conversions in MDR over 10%Co/MA and 3%La−10%Co/MA at stoichiometry ratio.

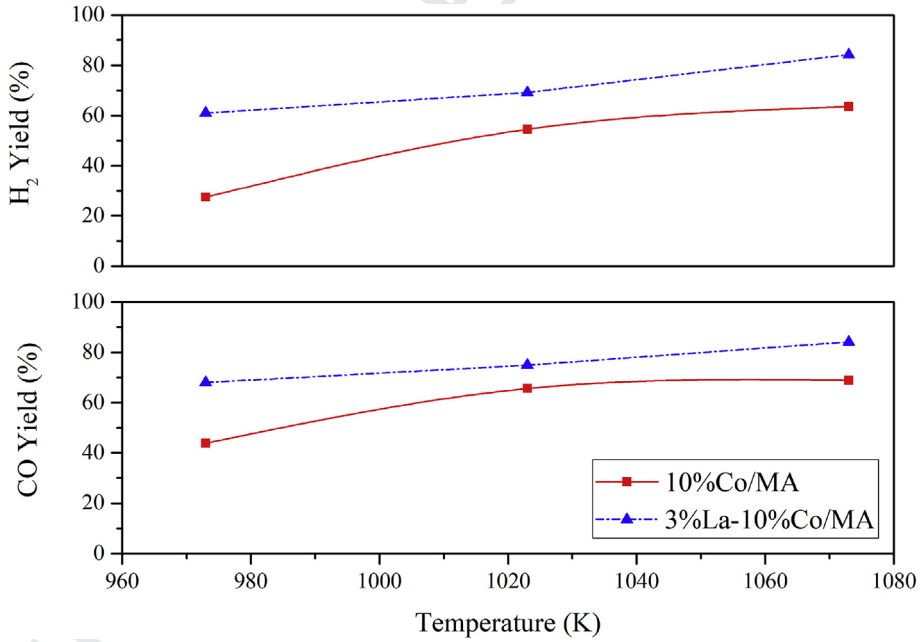

Fig. 4. Effect of temperature on CO and H_2 yields in MDR over 10%Co/MA and 3%La−10%Co/MA at stoichiometry ratio.

3.3. Spent catalyst characterization

3.3.1. XRD analyses

The crystallography of spent catalysts collected from MDR runs at 1023 K was also assessed by XRD (see Fig. 7). For both samples, the strong peak appearing at 2θ of 26.3° confirmed the existence of well-crystallized graphite (JCPDS card No. 75−0444), inevitably formed by CH_4 disproportion at high temperature [43]. The crystallite size of graphite on spent 10%Co/MA and 3%La−10%Co/MA was about 5.0 and 6.6 nm, correspondingly. Though all Co^{3+} and Co^{2+} particles were reduced to cobalt metallic form in H_2 activation prior to MDR run, the Co (0) signal at 2θ of 51.5° (JCPDS card No. 15−0806) and identified peaks (37.2° and 44.5°) of Co_3O_4 phase were found in both patterns of used catalysts. It could be due to the partial Co^0 re-oxidation during air-exposure when the samples were discharged from the reactor for XRD measurement [20].

3.3.2. Raman measurements

The Raman scattering of virgin and spent samples was performed to inspect the carbonaceous deposits on used catalysts after

Please cite this article as: N.T. Tran et al., La-doped cobalt supported on mesoporous alumina catalysts for improved methane dry reforming and coke mitigation, Journal of the Energy Institute, https://doi.org/10.1016/j.joei.2020.01.019

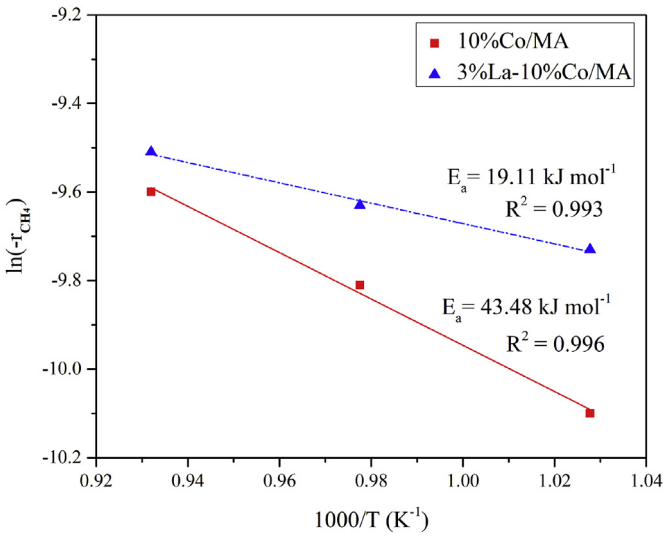

Fig. 5. Arrhenius plots for activation energy estimation of MDR over 10%Co/MA and 3%La−10%Co/MA.

MDR at 1023 K as illustrated in Fig. 8. Both virgin catalysts disclosed the presence of Co_3O_4 phase with typical peaks at about 474, 518, 610 and 679 cm^{-1} (see Fig. 8(a) and (b)) in line with XRD patterns (cf. Fig. 1). Like XRD measurements, La_2O_3 phase owning characteristic bands at 280, 342, and 446 cm^{-1} [44] was not evident in Raman spectra of all catalysts most likely because of well-dispersed La_2O_3 nanoparticles with smaller crystalline size than the Raman detection limits [20]. Thus, XPS analysis was used for the verification of La_2O_3 presence and discussed later in Section 3.3.4. For used catalysts, the typical peaks corresponding to the vibrational modes of Co_3O_4 were not observed within Raman shift range of 450−700 cm^{-1} (see Fig. 8(c) and (d)) although this phase was previously detected through XRD measurements. This could suggest that the extent of Co^0 to Co_3O_4 re-oxidation owing to air-exposure was small and hence it could not be identified by Raman spectroscopy.

As seen in the Raman spectra of spent catalysts (Fig. 8(c) and (d)), the discrete Raman shifts at 1339 and 1574 cm^{-1} were attributed to D-band (defect carbon) and G-band (graphitic carbon). The D-band arose from the vibration modes of amorphous sp^3-bonded carbon (C−C) network whereas sp^2-hybridized graphitic carbon atoms (C=C) were evidenced with G-band detection [45]. Thus, the appearance of D- and G-bands verified the co-existence of amorphous carbon (or filamentous carbon) and graphite [46].

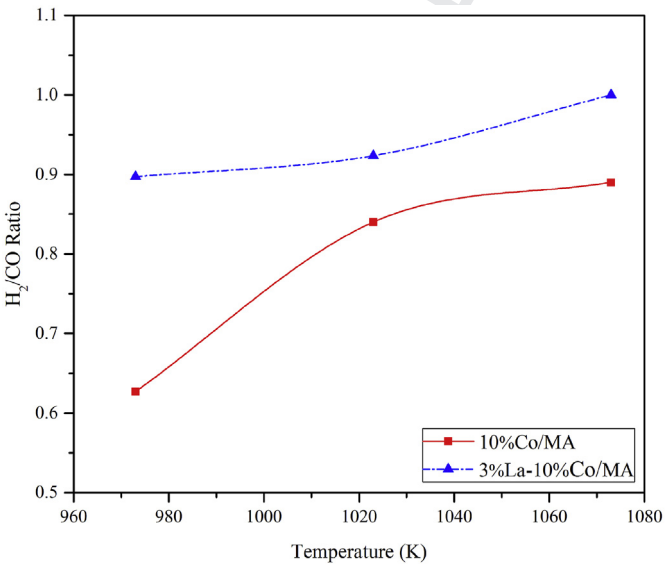

Fig. 6. Effect of temperature on H_2/CO ratio in MDR over 10%Co/MA and 3%La−10%Co/MA at stoichiometry ratio.

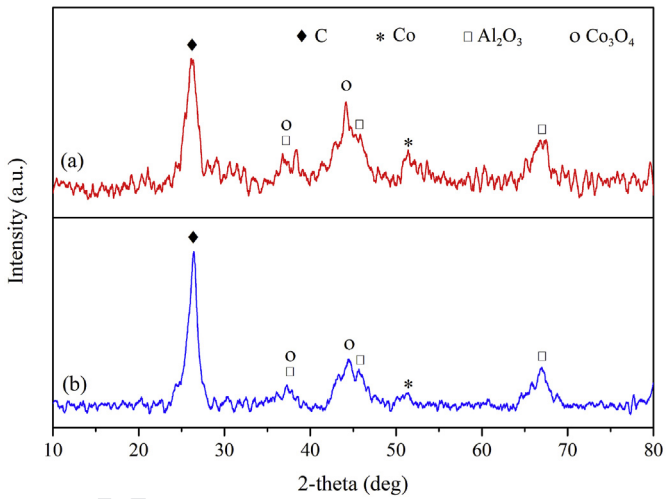

Fig. 7. XRD patterns for spent (a) 10%Co/MA, and (b) 3%La−10%Co/MA after MDR at 1023 K.

3.3.3. Thermal programmed oxidation measurements

The quantity and rate of accumulated carbon formation at different temperatures were accurately determined via TPO results as illustrated in Fig. 9. The behavior of deposited carbon formation (i.e., percentage and rate of deposited carbon) with respect to reforming temperature showed an open-downward parabolic shape for both used catalysts. At 973 K, there were about 27.9% and 23.0% carbon formed on 10%Co/MA and 3%La−10%Co/MA catalyst surface, respectively. As the temperature reached to 1023 K, these values noticeably increased to 47.7% and 35.5% for the corresponding 10%Co/MA and 3%La−10%Co/MA as a result of

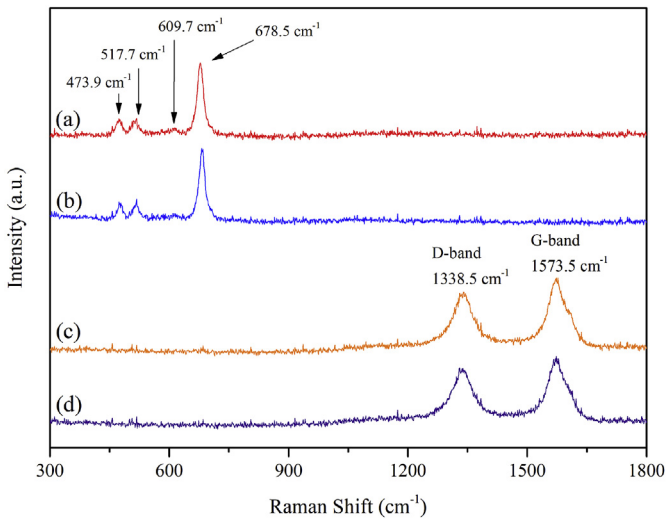

Fig. 8. Raman spectra of (a) fresh 10%Co/MA, (b) fresh 3%La−10%Co/MA, (c) spent 10%Co/MA, and (d) spent 3%La−10%Co/MA after MDR at 1023 K.

Please cite this article as: N.T. Tran et al., La-doped cobalt supported on mesoporous alumina catalysts for improved methane dry reforming and coke mitigation, Journal of the Energy Institute, https://doi.org/10.1016/j.joei.2020.01.019

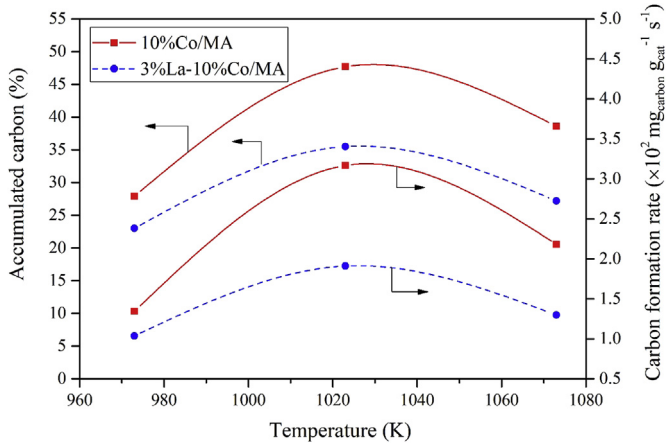

Fig. 9. Carbon formation on spent 10%Co/MA and 3%La−10%Co/MA after MDR at 973 K, 1023 K, and 1073 K.

intensifying extent of endothermic methane disproportion. However, the opposite trend was observed at elevated reaction temperature of 1073 K, which was attributed to the rising rate of reverse Boudouard reaction (see Eq. (11)) for deposited carbon elimination.

$$C + CO_2 \rightleftarrows 2CO \qquad (\Delta H_{298\ K} = +172\ \text{kJ mol}^{-1}) \qquad (11)$$

As seen in Fig. 9, the amount of carbons on spent 3%La−10%Co/MA was always less than that of used 10%Co/MA about 17−30% depending on temperature. The positive effect of La_2O_3 promotion was accounted for the reduction in carbon deposition. Indeed, the basic nature of La_2O_3 could attract more CO_2 adsorption for gasifying surface C_xH_y carbonaceous species [19]. In addition, the smaller crystalline size of 3%La−10%Co/MA was allegedly responsible for carbon resistance [47]. The oxidation of carbonaceous materials on promoted catalyst surface was also associated with the high oxygen mobility and redox character of La_2O_3 [48]. The great oxygen storage capacity of La_2O_3 could induce the formation of lanthanum dioxycarbonate ($La_2O_2CO_3$) transitional phase via the reaction between La_2O_3 and CO_2 and this intermediate form could subsequently eliminate C_xH_y species from catalyst surface as illustrated in Scheme 1.

3.3.4. X-ray photoelectron analyses

The XPS scans were conducted for used samples to examine the surface oxidation states and carbonaceous types. The binding energy (BE) in all spectra was adjusted based on the C 1s peak of adventitious carbon at 284.6 eV. The XPS narrow scan spectra for Co $2p_{3/2}$, C 1s, La 3d and O 1s are displayed in Figs. 10−13, respectively whilst the interpreation of binding energy is summarized in Table 3.

Fig. 10 shows that the expanded Co $2p_{3/2}$ spectra of spent catalysts were deconvoluted into four peaks using Gaussian algorithm in OriginPro 2016 software. As summarized in Table 3, the Gaussian peaks were observed at BEs of 778.0−778.9, 779.6−780.4, 781.4−782.2 and 786.4−786.5 eV, belonging to the metallic Co^0, Co_3O_4 oxide, $CoAl_2O_4$ spinel phases and a satellite shake-up band in this order [49,50]. The co-existence of various Co and Co oxide species is in line with XRD results (cf. Fig. 1). It is noteworthy to mention that all cleaved peaks of Co $2p_{3/2}$ narrow scan on La-promoted specimen located at lower BE values than those of the un-promoted counterpart. This could confirm the enriched electron density over cobalt particles induced by electron-donating La_2O_3 promoter [20,56]. Hence, the electron-rich environment on 3% La−10%Co/MA alleviated the H_2 reduction process as aforementioned in H_2-TPR (cf. Fig. 2).

The enlarged C 1s XPS spectra (Fig. 11) demonstrated the co-presence of graphitic carbon and amorphous carbon in line with the above-mentioned Raman results (i.e., G-band and D-band, respectively as given in Fig. 8). In particular, the peak at BE of 284.6 eV was assigned to graphitic carbon whilst amorphous carbon was depicted with the broad BE signal at around 286 eV [57,58].

Interestingly, the La 3d XPS detailed scan of spent 3%La−10%Co/MA (see Fig. 12) revealed two doublet peaks with BE gap of about 16.8 eV typical value for La^{3+} [55]. These doublet peaks correspond to La $3d_{3/2}$ (BE of 851.9 eV) and La $3d_{5/2}$ (BE of 835.1 eV) belonging to lattice lanthanum in intermediate $La_2O_2CO_3$ form on catalyst surface [55]. The detection of this intermediate phase formed by La_2O_3 and CO_2 reaction would convincingly prove the simultaneous carbon gasification in MDR through the *in situ* redox and oxidation cycle of $La_2O_2CO_3$ ↔ La_2O_3 as illustrated in Scheme 1. It is noteworthy to mention that unlike XPS analysis, the XRD pattern of spent 3%La−10%Co/MA (cf. Fig. 7) do not identify the formation of lanthanum dioxycarbonate possessing the characteristic diffraction peaks at 2θ: 13.1°, 22.8°, 29.6°, 30.8°, 41.1° and 44.5° (JCPDS card No. 22−1127) [59]. It could be assigned to the low sensitivity of XRD measurement induced by small $La_2O_2CO_3$ crystallite size and low La loading.

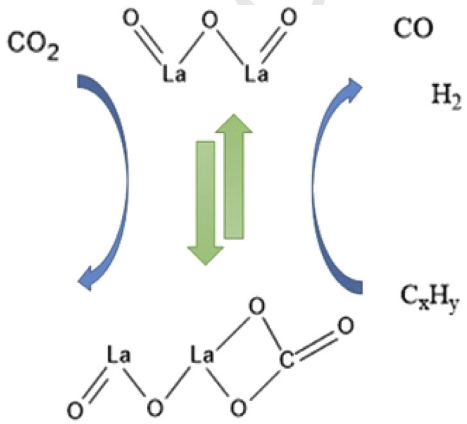

Scheme 1. La_2O_3 redox cycle for surface carbon removal during MDR.

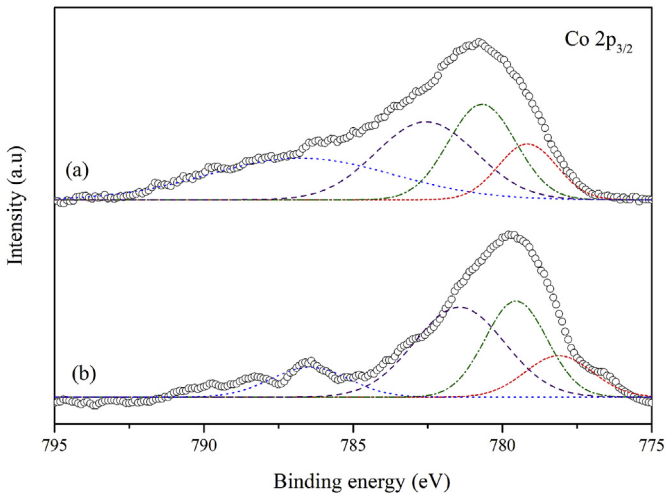

Fig. 10. Co $2p_{3/2}$ XPS spectra for spent (a) 10%Co/MA and (b) 3%La−10%Co/MA after MDR at 1023 K.

Please cite this article as: N.T. Tran et al., La-doped cobalt supported on mesoporous alumina catalysts for improved methane dry reforming and coke mitigation, Journal of the Energy Institute, https://doi.org/10.1016/j.joei.2020.01.019

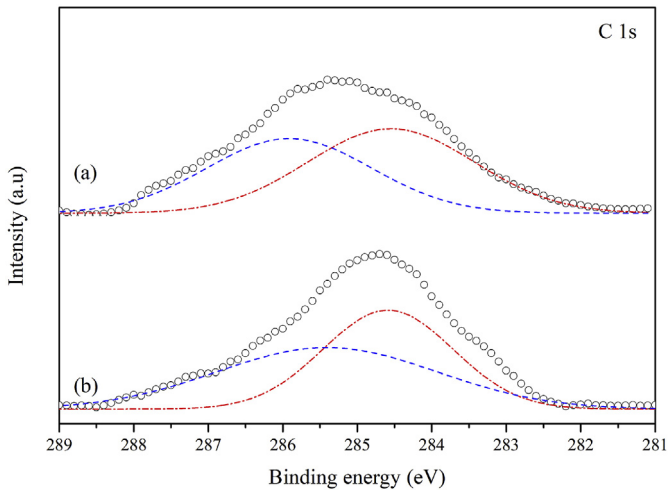

Fig. 11. C 1 s XPS spectra for spent (a) 10%Co/MA and (b) 3%La−10%Co/MA after MDR at 1023 K.

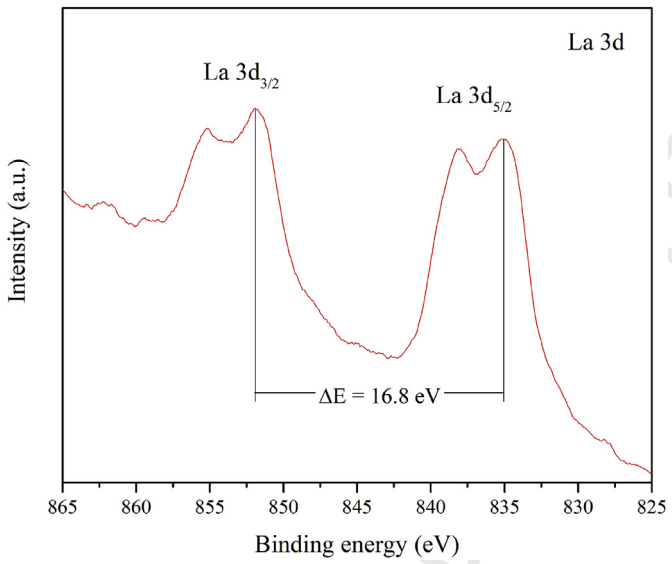

Fig. 12. La 3d XPS spectrum for spent 3%La−10%Co/MA after MDR at 1023 K.

The mobile oxygen vacancy of catalysts is a key factor determining the degree of carbon removal from catalyst surface as it is the preferred site for the adsorption of CO_2 oxidizing agent. The mobile oxygen vacancy was evaluated based on the O 1s XPS signal as shown in Fig. 13. The surface lattice oxygen atoms from Co_3O_4 and Al_2O_3 forms were detected at BE around 529.6−529.7 eV (peak II) whilst the deconvoluted peak I at 531.0−531.5 eV matched to the surface adsorbed oxygen species in carbonate compounds induced by oxygen vacancies in catalysts [60]. Hence, the degree of oxygen vacancies, $D_{O\text{-}Vac}$ (%) could be quantified via the relative amount of adsorbed oxygen in spent catalysts as expressed in Eq. (12) [61].

$$D_{O-Vac}(\%) = \frac{O_{Ads}}{(O_{Lat} + O_{Ads})} \times 100\% \quad (12)$$

where O_{Ads} and O_{Lat}, in turn, belong to the integral areas of peaks I and II (see Fig. 13).

The oxygen vacancy degree of spent 3%La−10%Co/MA was about 73.3%, which was 1.4 times higher than that of the spent

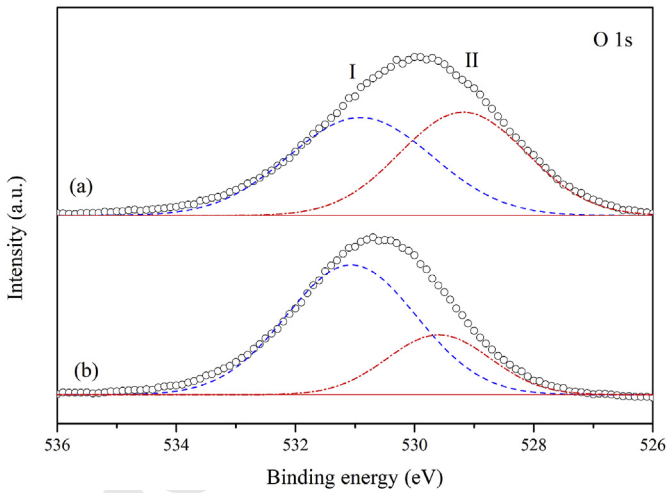

Fig. 13. O 1s XPS spectra for spent (a) 10%Co/MA and (b) 3%La−10%Co/MA after MDR at 1023 K.

unpromoted counterpart (51.8%). Interestingly, the increasing $D_{O\text{-}Vac}$ value of 1.4 times with La_2O_3 addition was also close to the magnification of decreasing carbon deposition (up to 1.3 times). This further confirms that La_2O_3 promotion hindered carbonaceous deposits, and oxygen vacancy degree was one of the main factors responsible for surface carbon removal.

3.3.5. HRTEM surface morphology study

The HRTEM analyses of fresh and spent catalysts are presented in Fig. 14. The relatively uniform and filamentous feature of MA support was apparently evident for both fresh catalysts and these MA filaments were adhered together as seen in Fig. 14(a) and (b). The tiny and dark spots labelled with yellow circles (Fig. 14(a)) could demonstrate the presence of Co nanoparticles. Interestingly, these nanoparticles were randomly dispersed on catalyst surface without agglomeration although catalysts were previously calcined at high temperature of 873 K. The thermal agglomeration resistance could be due to the strong interaction between Al_2O_3 nanofilament and Co metal. Thus, it could impede the movement of Co nanocrystals to form large particles under thermal treatment. The absence of un-favored metal accumulation could also contribute to result in a great catalytic activity with reactant conversions of more than 90% in this work. As seen in Fig. 14(c) and (d), the unavoidable amorphous carbon and graphite were clearly spotted on used catalysts corroborated with Raman (see Fig. 8) and XPS (see Fig. 11) results because of thermally preferred CH_4 decomposition in agreement with other studies [46].

4. Conclusions

The role of La_2O_3 promoter in the enhanced performance and coke resistance of 10%Co/MA for MDR was investigated. The Co_3O_4 and $CoAl_2O_4$ phases were formed on the catalyst surface, whereas the highly dispersed La_2O_3 demonstrated a small crystallite size of 8−10 nm. H_2 reduction was also facilitated with La_2O_3 addition, thereby increasing the amount of Co^0 active sites for greater catalytic performance. Regardless of the reaction temperatures, La-promoted catalyst not only showed a higher MDR activity but also yielded less deposited carbon as compared with un-promoted cobalt catalyst. In particular, La_2O_3 addition could enhance CH_4 and CO_2 conversions up to 93.7% and 93.2%, respectively at 1073 K reasonably because of the smaller Co_3O_4 crystallite size, eased H_2-reduction and rising basic character. The formation of $La_2O_2CO_3$

Please cite this article as: N.T. Tran et al., La-doped cobalt supported on mesoporous alumina catalysts for improved methane dry reforming and coke mitigation, Journal of the Energy Institute, https://doi.org/10.1016/j.joei.2020.01.019

Table 3
Summary of XPS peaks assignments for used catalysts after MDR at 1023 K.

XPS peak	Binding energy (eV)		Assignment	Ref.
	10%Co/MA	3%La−10%Co/MA		
Co $2p_{3/2}$	786.5	786.4	Satellite peak	[49]
	782.2	781.4	$CoAl_2O_4$	[49]
	780.4	779.6	Co_3O_4	[50]
	778.9	778.0	Co (0)	[50]
C 1s	285.7	285.6	Amorphous carbon	[51,52]
	284.6	284.6	Graphitic carbon	[52,53]
O 1s	531.5	531.0	Adsorbed oxygen species	[20,54]
	529.7	529.6	Surface lattice oxygen in Al_2O_3 and/or Co_3O_4	[20,54]
La $3d_{3/2}$	–	851.9	$La_2O_2CO_3$	[55]
La $3d_{5/2}$	–	835.1		

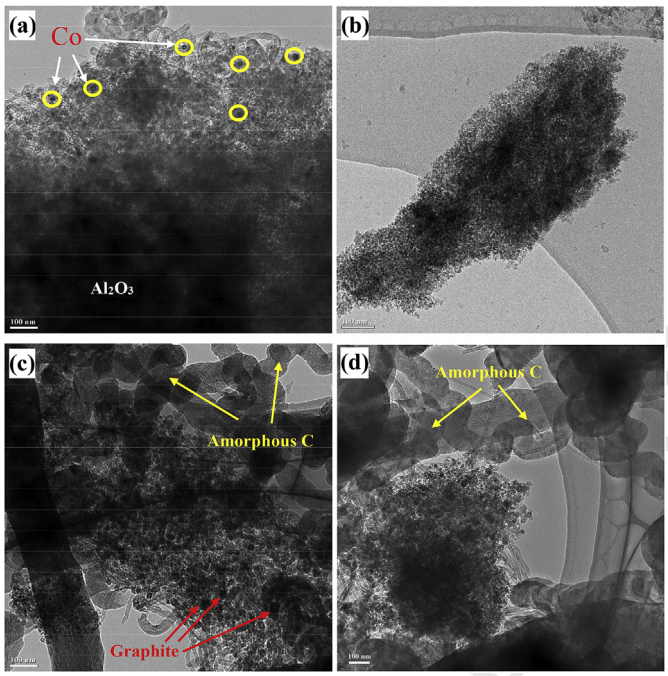

Fig. 14. HRTEM images of (a) fresh 10%Co/MA, (b) fresh 3%La−10%Co/MA, (c) spent 10% Co/MA, and (d) spent 3%La−10%Co/MA after MDR at 1023 K.

intermediate phase from the *in situ* interaction of La_2O_3 with CO_2 during MDR was confirmed by XPS analysis and this form could induce the efficient elimination of surface C_xH_y species from the catalyst. Even though amorphous and graphitic carbons were unavoidably formed on spent catalysts due to CH_4 decomposition, the amount of carbonaceous species was reduced significantly with La_2O_3 addition (17−30%) owing to its redox cycle and superior degree of oxygen vacancy (73.3%). The MDR on fibrous Al_2O_3-supported Co catalysts exhibited ideal H_2/CO ratios from 0.63 to 0.99 preferred for Fischer-Tropsch synthesis.

Acknowledgement

The authors would like to acknowledge the financial support from IUH Research Grant Scheme (44/HĐ-ĐHCN) provided by Industrial University of Ho Chi Minh City, Vietnam to conduct this study.

Appendix A. Supplementary data

Supplementary data to this article can be found online at https://doi.org/10.1016/j.joei.2020.01.019.

References

[1] A. Forte, A. Zucaro, S. Faugno, R. Basosi, A. Fierro, Carbon footprint and fossil energy consumption of bio-ethanol fuel production from Arundo donax L. crops on marginal lands of Southern Italy, Energy 150 (2018) 222−235, https://doi.org/10.1016/j.energy.2018.02.030.
[2] S.A.R. Khan Sar, Y. Zhang, M. Anees, H. Golpîra, A. Lahmar, D. Qianli, Green supply chain management, economic growth and environment: a GMM based evidence, J. Clean. Prod. 185 (2018) 588−599, https://doi.org/10.1016/j.jclepro.2018.02.226.
[3] J. Kataria, S. Mohapatra, K. Kundu, Biodiesel production from waste cooking oil using heterogeneous catalysts and its operational characteristics on variable compression ratio CI engine, J. Energy Inst. 92 (2019) 275−287, https://doi.org/10.1016/j.joei.2018.01.008.
[4] N.A.K. Aramouni, J.G. Touma, B.A. Tarboush, J. Zeaiter, M.N. Ahmad, Catalyst design for dry reforming of methane: analysis review, Renew. Sustain. Energy Rev. 82 (2018) 2570−2585, https://doi.org/10.1016/j.rser.2017.09.076.
[5] S. Mao, Z. Tan, L. Zhang, Q. Huang, Plasma-assisted biogas reforming to syngas at room temperature condition, J. Energy Inst. 91 (2018) 172−183, https://doi.org/10.1016/j.joei.2017.01.003.
[6] S. Basu, N.C. Pradhan, Steam reforming of acetone over NiCoMgAl mixed oxide catalysts obtained from hydrotalcite precursors, Int. J. Hydrogen Energy (2020), https://doi.org/10.1016/j.ijhydene.2019.04.173. In press. Q4
[7] T.S. Zeleke, M.C. Tsai, M.A. Weret, C.J. Huang, M.K. Birhanu, T.C. Liu, C.P. Huang, Y.L. Soo, Y.W. Yang, W.N. Su, Immobilized single molecular molybdenum disulfide on carbonized polyacrylonitrile for hydrogen evolution reaction, ACS Nano 13 (2019) 6720−6729, https://doi.org/10.1021/acsnano.9b01266.
[8] J. Dobosz, M. Małecka, M. Zawadzki, Hydrogen generation via ethanol steam reforming over Co/HAp catalysts, J. Energy Inst. 91 (2018) 411−423, https://doi.org/10.1016/j.joei.2017.02.001.
[9] F. Polo-Garzon, D. Pakhare, J.J. Spivey, D.A. Bruce, Dry reforming of methane on Rh-doped pyrochlore catalysts: a steady-state isotopic transient kinetic study, ACS Catal. 6 (2016) 3826−3833, https://doi.org/10.1021/acscatal.6b00666.
[10] M.S. Aw, M. Zorko, I.G. Osojnik Crnivec, A. Pintar, Progress in the synthesis of catalyst supports: synergistic effects of nanocomposites for attaining long-term stable activity in CH_4-CO_2 dry reforming, Ind. Eng. Chem. Res. 54 (2015) 3775−3787, https://doi.org/10.1021/acs.iecr.5b00134.
[11] J.H. Park, S. Yeo, T.J. Kang, H.R. Shin, I. Heo, T.S. Chang, Effect of Zn promoter on catalytic activity and stability of Co/ZrO_2 catalyst for dry reforming of CH_4, J. CO_2 Util. 23 (2018) 10−19, https://doi.org/10.1016/j.jcou.2017.11.002.
[12] S. Arora, R. Prasad, An overview on dry reforming of methane: strategies to reduce carbonaceous deactivation of catalysts, RSC Adv. 6 (2016) 108668−108688, https://doi.org/10.1039/C6RA20450C.
[13] H. Ay, D. Üner, Dry reforming of methane over CeO_2 supported Ni, Co and Ni-Co catalysts, Appl. Catal. B Environ. 179 (2015) 128−138, https://doi.org/10.1016/j.apcatb.2015.05.013.
[14] T.S. Phan, A.R. Sane, B.R. de Vasconcelos, A. Nzihou, P. Sharrock, D. Grouset, D.P. Minh, Hydroxyapatite supported bimetallic cobalt and nickel catalysts for syngas production from dry reforming of methane, Appl. Catal. B Environ. 224 (2018) 310−321, https://doi.org/10.1016/j.apcatb.2017.10.063.
[15] J.H. Park, S. Yeo, T.J. Kang, I. Heo, K.Y. Lee, T.S. Chang, Enhanced stability of Co catalysts supported on phosphorus-modified Al_2O_3 for dry reforming of CH_4, Fuel 212 (2018) 77−87, https://doi.org/10.1016/j.fuel.2017.09.090.
[16] Q. Ma, J. Sun, X. Gao, J. Zhang, T. Zhao, Y. Yoneyama, N. Tsubaki, Ordered mesoporous alumina-supported bimetallic Pd-Ni catalysts for methane dry reforming reaction, Catal. Sci. Technol. 6 (2016) 6542−6550, https://doi.org/10.1039/C6CY00841K.
[17] S. Singh, R. Kumar, H.D. Setiabudi, S. Nanda, D.V.N. Vo, Advanced synthesis strategies of mesoporous SBA-15 supported catalysts for catalytic reforming applications: a state-of-the-art review, Appl. Catal. Gen. 559 (2018) 57−74, https://doi.org/10.1016/j.apcata.2018.04.015.
[18] H. Drobná, M. Kout, A. Sołtysek, V.M. González-Delacruz, A. Caballero, L. Čapek, Analysis of Ni species formed on zeolites, mesoporous silica and

Please cite this article as: N.T. Tran et al., La-doped cobalt supported on mesoporous alumina catalysts for improved methane dry reforming and coke mitigation, Journal of the Energy Institute, https://doi.org/10.1016/j.joei.2020.01.019

alumina supports and their catalytic behavior in the dry reforming of methane, React. Kinet. Mech. Catal. 121 (2017) 255–274, https://doi.org/10.1007/s11144-017-1149-3.

[19] M.B. Bahari, N.H.H. Phuc, F. Alenazey, K.B. Vu, N. Ainirazali, D.V.N. Vo, Catalytic performance of La-Ni/Al_2O_3 catalyst for CO_2 reforming of ethanol, Catal. Today 291 (2017) 67–75, https://doi.org/10.1016/j.cattod.2017.02.019.

[20] F. Fayaz, L.G. Bach, M.B. Bahari, T.D. Nguyen, K.B. Vu, R. Kanthasamy, C. Samart, C. Nguyen-Huy, D.V.N. Vo, Stability evaluation of ethanol dry reforming on Lanthania-doped cobalt-based catalysts for hydrogen-rich syngas generation, Int. J. Energy Res. 43 (2019) 405–416, https://doi.org/10.1002/er.4274.

[21] F. Fayaz, H.T. Danh, C. Nguyen-Huy, K.B. Vu, B. Abdullah, D.V.N. Vo, Promotional effect of Ce-dopant on Al_2O_3-supported Co catalysts for syngas production via CO_2 reforming of ethanol, Procedia Eng 148 (2016) 646–653, https://doi.org/10.1016/j.proeng.2016.06.530.

[22] M.B. Bahari, B.C. Goo, T.L. Pham, T.J. Siang, H.T. Danh, N. Ainirazali, D.V.N. Vo, Hydrogen-rich syngas production from ethanol dry reforming on La-doped Ni/Al_2O_3 catalysts: effect of promoter loading, Procedia Eng 148 (2016) 654–661, https://doi.org/10.1016/j.proeng.2016.06.531.

[23] JCPDS Powder Diffraction File, International Centre for Diffraction Data, PA: Swarthmore, 2000.

[24] A.L. Patterson, The Scherrer formula for X-ray particle size determination, Phys. Rev. 56 (1939) 978–982, https://doi.org/10.1103/PhysRev.56.978.

[25] Y. Feng, H. Zhang, L. Fang, W. Li, Y. Wang, Novel three-dimensional flower-like porous Al_2O_3 nanosheets anchoring hollow NiO nanoparticles for high-efficiency lithium ion batteries, J. Mater. Chem. 4 (2016) 11507–11515, https://doi.org/10.1039/C6TA04323B.

[26] S.Z. Mohammadi, H. Beitollahi, H. Allahabadi, T. Rohani, Disposable electrochemical sensor based on modified screen printed electrode for sensitive cabergoline quantification, J. Electroanal. Chem. 847 (2019), https://doi.org/10.1016/j.jelechem.2019.113223, 113223.

[27] M. Espitia-Sibaja, M. Muñoz, S. Moreno, R. Molina, Effects of the cobalt content of catalysts prepared from hydrotalcites synthesized by ultrasound-assisted coprecipitation on hydrogen production by oxidative steam reforming of ethanol (OSRE), Fuel 194 (2017) 7–16, https://doi.org/10.1016/j.fuel.2016.12.086.

[28] G. Velciu, A. Melinescu, V. Marinescu, M. Preda, $LaCoO_3$ synthesis by intensive mechanical activation, Ceram. Int. 41 (2015) 6876–6881, https://doi.org/10.1016/j.ceramint.2015.01.138.

[29] S.A. Kondrat, P.J. Smith, L. Lu, J.K. Bartley, S.H. Taylor, M.S. Spencer, G.J. Kelly, C.W. Park, C.J. Kiely, G.J. Hutchings, Preparation of a highly active ternary Cu-Zn-Al oxide methanol synthesis catalyst by supercritical CO_2 anti-solvent precipitation, Catal. Today 317 (2018) 12–20, https://doi.org/10.1016/j.cattod.2018.03.046.

[30] D. San José-Alonso, M.J. Illán-Gómez, M.C. Román-Martínez, Low metal content Co and Ni alumina supported catalysts for the CO_2 reforming of methane, Int. J. Hydrogen Energy 38 (2013) 2230–2239, https://doi.org/10.1016/j.ijhydene.2012.11.080.

[31] M.B. Durán-Guevara, J. Ortiz-Landeros, H. Pfeiffer, M.I. Espitia-Cabrera, M.E. Contreras-García, Potassium-based sorbents using mesostructured γ-alumina supports for low temperature CO_2 capture, Ceram. Int. 41 (2015) 3036–3044, https://doi.org/10.1016/j.ceramint.2014.10.140.

[32] F. Fayaz, N.T.A. Nga, T.L.M. Pham, H.T. Danh, B. Abdullah, H.D. Setiabudi, D.V.N. Vo, Hydrogen production from ethanol dry reforming over lanthania-promoted Co/Al_2O_3 catalyst, IIUM Eng. J. 19 (2018) 24–33, https://doi.org/10.31436/iiumej.v19i1.813.

[33] W. Cai, Y. Hu, J. Chen, G. Zhang, T. Xia, Synthesis of nanorod-like mesoporous γ-Al_2O_3 with enhanced affinity towards Congo red removal: effects of anions and structure-directing agents, CrystEngComm 14 (2012) 972–977. https://10.1039/C1CE05975K.

[34] A. Jean-Marie, A. Griboval-Constant, A.Y. Khodakov, E. Monflier, F. Diehl, β-Cyclodextrin for design of alumina supported cobalt catalysts efficient in Fischer–Tropsch synthesis, Chem. Commun. 47 (2011) 10767–10769, https://doi.org/10.1039/C1CC13800F.

[35] G. Zhi, X. Guo, Y. Wang, G. Jin, Effect of La_2O_3 modification on the catalytic performance of Ni/SiC for methanation of carbon dioxide, Catal. Commun. 16 (2011) 56–59, https://doi.org/10.1016/j.catcom.2011.08.037.

[36] Y. Gong, J. Wu, M. Kitano, J. Wang, T.N. Ye, J. Li, Y. Kobayashi, K. Kishida, H. Abe, Y. Niwa, Ternary intermetallic LaCoSi as a catalyst for N_2 activation, Nat 1 (2018) 178–185, https://doi.org/10.1038/s41929-017-0022-0.

[37] O. Omoregbe, H.T. Danh, C. Nguyen-Huy, H.D. Setiabudi, S.Z. Abidin, Q.D. Truong, D.V.N. Vo, Syngas production from methane dry reforming over Ni/SBA-15 catalyst: effect of operating parameters, Int. J. Hydrogen Energy 42 (2017) 11283–11294, https://doi.org/10.1016/j.ijhydene.2017.03.146.

[38] B.V. Ayodele, M.R. Khan, S.S. Lam, C.K. Cheng, Production of CO-rich hydrogen from methane dry reforming over lanthania-supported cobalt catalyst: kinetic and mechanistic studies, Int. J. Hydrogen Energy 41 (2016) 4603–4615, https://doi.org/10.1016/j.ijhydene.2016.01.091.

[39] S. Sato, R. Takahashi, M. Kobune, H. Gotoh, Basic properties of rare earth oxides, Appl. Catal. Gen. 356 (2009) 57–63, https://doi.org/10.1016/j.apcata.2008.12.019.

[40] L.N. Bobrova, A.S. Bobin, N.V. Mezentseva, V.A. Sadykov, J.W. Thybaut, G.B. Marin, Kinetic assessment of dry reforming of methane on Pt+Ni containing composite of fluorite-like structure, Appl. Catal. B Environ. 182 (2016) 513–524, https://doi.org/10.1016/j.apcatb.2015.09.049.

[41] T.J. Siang, S. Singh, O. Omoregbe, L.G. Bach, H.H.N. Phuc, D.V.N. Vo, Hydrogen production from CH_4 dry reforming over bimetallic Ni-Co/Al_2O_3 catalyst, J. Energy Inst. 91 (2018) 683–694, https://doi.org/10.1016/j.joei.2017.06.001.

[42] D.V.N. Vo, C.G. Cooper, T.H. Nguyen, A.A. Adesina, D.B. Bukur, Evaluation of alumina-supported Mo carbide produced via propane carburization for the Fischer-Tropsch synthesis, Fuel 93 (2012) 105–116, https://doi.org/10.1016/j.fuel.2011.10.015.

[43] L. Guczi, G. Stefler, O. Geszti, I. Sajó, Z. Pászti, A. Tompos, Z. Schay, Methane dry reforming with CO_2: a study on surface carbon species, Appl. Catal. Gen. 375 (2010) 236–246, https://doi.org/10.1016/j.apcata.2009.12.040.

[44] N.N. Wang, Y. Wang, H.F. Cheng, Z. Tao, J. Wang, W.Z. Wu, Impact of cationic lanthanum species on zeolite Y: an infrared, excess infrared and Raman spectroscopic study, RSC Adv. 3 (2013) 20237–20245, https://doi.org/10.1039/C3RA42634C.

[45] X. Hu, J. Jia, G. Wang, J. Chen, H. Zhan, Z. Wen, Reliable and general route to inverse opal structured nanohybrids of carbon-confined transition metal sulfides quantum dots for high-performance sodium storage, Adv. Energy Mater. 8 (2018), https://doi.org/10.1002/aenm.201801452, 1801452.

[46] N.D. Charisiou, L. Tzounis, V. Sebastian, S.J. Hinder, M.A. Baker, K. Polychronopoulou, M.A. Goula, Investigating the correlation between deactivation and the carbon deposited on the surface of Ni/Al_2O_3 and Ni/La_2O_3-Al_2O_3 catalysts during the biogas reforming reaction, Appl. Surf. Sci. 474 (2019) 42–56, https://doi.org/10.1016/j.apsusc.2018.05.177.

[47] M. Usman, W.M.A.W. Daud, H.F. Abbas, Dry reforming of methane: influence of process parameters: a review, Renew. Sustain. Energy Rev. 45 (2015) 710–744, https://doi.org/10.1016/j.rser.2015.02.026.

[48] K. Li, X. Chang, C. Pei, X. Li, S. Chen, X. Zhang, S. Assabumrungrat, Z.J. Zhao, L. Zeng, J. Gong, Ordered mesoporous Ni/La_2O_3 catalysts with interfacial synergism towards CO_2 activation in dry reforming of methane, Appl. Catal. B Environ. 259 (2019), https://doi.org/10.1016/j.apcatb.2019.118092, 118092.

[49] C.M. Álvarez-Docio, J.J. Reinosa, A. Del Campo, J.F. Fernández, Investigation of thermal stability of 2D and 3D $CoAl_2O_4$ particles in core-shell nanostructures by Raman spectroscopy, J. Alloys Compd. 779 (2019) 244–254, https://doi.org/10.1016/j.jallcom.2018.11.263.

[50] A.I. Paksoy, B.S. Caglayan, A.E. Aksoylu, A study on characterization and methane dry reforming performance of Co–Ce/ZrO_2 catalyst, Appl. Catal. B Environ. 168 (2015) 164–174, https://doi.org/10.1016/j.apcatb.2014.12.038.

[51] J.W. Long, M. Laskoski, G.W. Peterson, T.M. Keller, K.A. Pettigrew, B.J. Schindler, Metal-catalyzed graphitic nanostructures as sorbents for vapor-phase ammonia, J. Mater. Chem. 21 (2011) 3477–3484, https://doi.org/10.1039/C0JM03167D.

[52] J.L. Ewbank, L. Kovarik, C.C. Kenvin, C. Sievers, Effect of preparation methods on the performance of Co/Al_2O_3 catalysts for dry reforming of methane, Green Chem. 16 (2014) 885–896, https://doi.org/10.1039/C3GC41782D.

[53] Y. Cui, G. Zhang, Z. Lin, X. Wang, Condensed and low-defected graphitic carbon nitride with enhanced photocatalytic hydrogen evolution under visible light irradiation, Appl. Catal. B Environ. 181 (2016) 413–419, https://doi.org/10.1016/j.apcatb.2015.08.018.

[54] Y. Chen, D. Zhang, X. Wu, H. Wang, C. Zhang, W. Yang, Y. Chen, Epoxy/α-alumina nanocomposite with high electrical insulation performance, Prog. Nat. Sci.: Mater. 27 (2017) 574–581, https://doi.org/10.1016/j.pnsc.2017.09.003.

[55] G. Chen, B. Han, S. Deng, Y. Wang, Y. Wang, Lanthanum dioxide carbonate $La_2O_2CO_3$ nanorods as a sensing material for chemoresistive CO_2 gas sensor, Electrochim. Acta 127 (2014) 355–361, https://doi.org/10.1016/j.electacta.2014.02.075.

[56] Q. Guo, J. Huang, W. Qian, H. Zhang, H. Ma, W. Ying, Effect of lanthanum on Zr-Co/γ-Al_2O_3 catalysts for fischer–tropsch synthesis, Catal. Lett. 148 (2018) 2789–2798, https://doi.org/10.1007/s10562-018-2443-z.

[57] L. Liu, X. Ma, J. Li, Hydrogen production from ethanol steam reforming over Ni/SiO_2 catalysts: a comparative study of traditional preparation and microwave modification methods, Int. J. Energy Res. 38 (2014) 860–874, https://doi.org/10.1002/er.3073.

[58] X. Zhao, H. Zhu, X. Yang, Amorphous carbon supported MoS_2 nanosheets as effective catalysts for electrocatalytic hydrogen evolution, Nanoscale 6 (2014) 10680–10685, https://doi.org/10.1039/C4NR01885K.

[59] D.Y. Kalai, K. Stangeland, Y. Jin, W.M. Tucho, Z. Yu, Biogas dry reforming for syngas production on La promoted hydrotalcite-derived Ni catalysts, Int. J. Hydrogen Energy 43 (2018) 19438–19450, https://doi.org/10.1016/j.ijhydene.2018.08.181.

[60] Y. Zhou, S. Li, J. Deng, L. Xiong, J. Wang, Y. Chen, Nanoscale heterogeneity and low-temperature redox property of CeO_2-ZrO_2-La_2O_3-Y_2O_3 quaternary solid solution, Mater. Chem. Phys. 208 (2018) 123–131, https://doi.org/10.1016/j.matchemphys.2018.01.004.

[61] N. Wang, K. Shen, L. Huang, X. Yu, W. Qian, W. Chu, Facile route for synthesizing ordered mesoporous Ni-Ce-Al oxide materials and their catalytic performance for methane dry reforming to hydrogen and syngas, ACS Catal. 3 (2013) 1638–1651, https://doi.org/10.1021/cs4003113.

Please cite this article as: N.T. Tran et al., La-doped cobalt supported on mesoporous alumina catalysts for improved methane dry reforming and coke mitigation, Journal of the Energy Institute, https://doi.org/10.1016/j.joei.2020.01.019